

Multi-task deep-learning optimization of trade-off properties for superior-performance Fe-based soft magnetic alloys

Kang-Yuan Li(李康源), Mao-Zhi Li(李茂枝), and Wei-Hua Wang(汪卫华)

Citation: Chin. Phys. B, 2026, 35 (**7**): 070705. DOI: 10.1088/1674-1056/ae5b5f
http://cpb.iphy.ac.cn; http://iopscience.iop.org/cpb

What follows is a list of articles you may be interested in

Polymer nanocomposites for electrocaloric refrigeration: Applications and research advances

Hongtian Li(黎洪天), Feifan Yang(杨非凡), Shenglin Jiang(姜胜林), Kanghua Li(李康华), and Guangzu Zhang(张光祖)
Chin. Phys. B, 2026, 35 (**7**): 070702. DOI: 10.1088/1674-1056/ae48ba

Electrocaloric thermal management devices: Toward high-efficiency solid-state refrigeration

Yiwen Bo(薄轶文) and Rujun Ma(马儒军)
Chin. Phys. B, 2026, 35 (**7**): 070701. DOI: 10.1088/1674-1056/ae3309

Thermal desorption characteristic of helium ion irradiated nickel-base alloy

Shasha Lv(吕沙沙), Rui Zhu(朱睿), Yumeng Zhao(赵雨梦), Mingyang Li(李明阳), Guojing Wang(王国景), Menglin Qiu(仇猛淋), Bin Liao(廖斌), Qingsong Hua(华青松), Jianping Cheng(程建平), Zhengcao Li(李正操)
Chin. Phys. B, 2020, 29 (**4**): 040704. DOI: 10.1088/1674-1056/ab7e99

Thermal characterization of GaN heteroepitaxies using ultraviolet transient thermoreflectance

Kang Liu(刘康), Jiwen Zhao(赵继文), Huarui Sun(孙华锐), Huaixin Guo(郭怀新), Bing Dai(代兵), Jiaqi Zhu(朱嘉琦)
Chin. Phys. B, 2019, 28 (**6**): 060701. DOI: 10.1088/1674-1056/28/6/060701

RAPID COMMUNICATION

Multi-task deep-learning optimization of trade-off properties for superior-performance Fe-based soft magnetic alloys

Kang-Yuan Li(李康源)[1], Mao-Zhi Li(李茂枝)[1,†], and Wei-Hua Wang(汪卫华)[2,3,4]

[1] *School of Physics and Key Laboratory of Quantum State Construction and Manipulation (Ministry of Education), Renmin University of China, Beijing 100872, China*

[2] *Songshan Lake Materials Laboratory, Dongguan* 523808, *China*

[3] *Institute of Physics, Chinese Academy of Sciences, Beijing* 100190, *China*

[4] *Center of Materials Science and Optoelectronics Engineering, University of Chinese Academy of Sciences, Beijing* 100049, *China*

(Received 2 March 2026; revised manuscript received 1 April 2026; accepted manuscript online 3 April 2026)

Fe-based amorphous alloys are promising soft magnetic materials for developing next-generation devices with high frequency and efficiency. However, optimizing Fe-based alloys with ultra-high saturation magnetic flux density (B_s), ultra-low coercivity (H_c), and good glass-forming ability remains a notorious challenge owing to the vast composition space and complex trade-offs among these properties. Thus, conventional design methods face great challenges. Here, we develop a generative multi-task deep learning (GMTDL) approach to achieve simultaneous optimization of compositions and trade-off properties. The GMTDL can sufficiently exploit and share knowledge from datasets across different tasks, despite the limitations and imbalances of these datasets. Therefore, it exhibits superior performance in predicting alloys with multiple targeted properties, outperforming previous machine learning-based design strategies. Moreover, the GMTDL can also tailor compositions, providing an efficient way to regulate properties and generate desired candidates for further experimental processing. The validity and reliability of GMTDL are rigorously tested by benchmarking against Fe-based alloys reported very recently. Moreover, some new alloys with ultra-high B_s and ultra-low H_c are predicted. The optimal content windows of key elements and their synergistic effects are also unraveled, providing practical guidance. Thus, our study establishes an effective and reliable paradigm for simultaneous prediction and optimization of high-performance materials with multiple properties.

Keywords: Fe-based amorphous alloys, soft magnetic materials, multi-task deep learning, multi-objective optimization, inverse design

PACS: 07.05.Mh, 75.50.Bb, 75.50.Kj, 75.60.Ej

DOI: 10.1088/1674-1056/ae5b5f **CSTR:** 32038.14.CPB.ae5b5f

1. Introduction

With the development of new infrastructure fields such as 5G communication, new energy vehicles, artificial intelligence, and intelligent manufacturing, it has become increasingly desirable to develop next-generation electrical equipment and electronic devices with high frequency, miniaturization, and high efficiency.[1,2] With increasing frequency, however, most of the electrical energy is consumed by magnetic components.[3,4] Thus, energy conversion efficiency associated with soft magnetic materials becomes a key factor in the development of high-frequency devices.[5] So far, silicon steels are the most widely used soft magnetic materials, yet they suffer from high core loss, low energy conversion efficiency, and consequently serious heating problems in devices when used at high frequencies such as megahertz frequencies.[6,7] While ferrites exhibit high permeability and low loss due to their high electrical resistivity, their low saturation magnetization is detrimental to the miniaturization of high-frequency devices.[8] Fe-based amorphous alloys have emerged as a promising new class of soft magnetic materials for high-frequency applications.[9] Compared to silicon steel, these alloys possess lower coercivity (H_c) and higher resistivity, which contribute to reduced core losses. Although the saturation magnetic flux density (B_s) of Fe-based amorphous alloys is relatively low, it can be improved by tuning the content of ferromagnetic elements and some other metallic and metalloid elements.[10,11] Moreover, the formation of nanocrystals within the amorphous matrix induced by heat treatment can further enhance the B_s.[12,13] Therefore, great efforts have been devoted to designing high-performance Fe-based alloys with high B_s, low H_c, and good glass-forming ability (GFA).[11,14]

However, the optimization and regulation of Fe-based alloys with ultra-high B_s, ultra-low H_c, and good GFA remain a notorious challenge.[11,14] While increasing the content of ferromagnetic elements favors the B_s, the GFA of these alloys rapidly decreases, leading to poor thermal stability and harsh and uncontrollable crystallization processes. To enhance the GFA, some metalloid elements, such as B, P, Si, and C, are of-

†Corresponding author. E-mail: maozhili@ruc.edu.cn

© 2026 Chinese Physical Society and IOP Publishing Ltd. All rights, including for text and data mining, AI training, and similar technologies, are reserved.

ten added, which mostly deteriorates the B_s. Meanwhile, minor additions of some metallic elements may be useful for controlling the nanocrystalline structure.[15] Moreover, there is also a trade-off between B_s and H_c, that is, enhancing B_s leads to deterioration of H_c.[16] Thus, it has been a long-standing challenge to balance the trade-offs among B_s, H_c, and GFA for optimizing high-performance Fe-based amorphous alloys, since this is essentially a high-dimensional search and optimization problem in a vast and highly complicated composition space integrating multiple properties.

So far, machine learning (ML) methods have been applied to accelerate the search for high-performance alloys.[17,18] However, such methods require manual input of alloy compositions. As alloy complexity increases, the number of potential compositions grows exponentially, rendering manual input impractical.[19] Very recently, rapid progress in generative approaches and autonomous laboratories (A-Labs) has provided efficient new strategies for addressing high-dimensional optimization problems and has significantly accelerated new material design.[20] Nevertheless, most existing A-Labs focus on single-objective design,[21,22] while practical applications mostly require simultaneous fulfillment of multiple performance objectives. This greatly increases the complexity of searching the performance space and finding optimal solutions.

To achieve multi-objective design, multiple single-task models are often developed for each individual property prediction, and step-by-step property screening is performed during the design procedure.[23–26] However, due to the diversity and complexity of alloy compositions and the scarcity of high-quality datasets, single-task models often face overfitting issues when applied to small datasets, which limits their practical performance. Recently, multi-task learning, a transfer learning strategy that shares information across multiple related tasks, has been shown to achieve multi-objective design by significantly enhancing model performance, including data augmentation, attention focusing, feature selection, and overfitting prevention.[27–30] For instance, Wu *et al.*[30] developed a multi-task learning model to successfully predict multiple properties of quantum many-body systems from short-range correlation data. Unlike crystalline materials, however, amorphous alloys are in non-equilibrium states; therefore, their disordered atomic structures are metastable and may not serve as reliable criteria for materials design. Moreover, the discovered Fe-based amorphous alloy compositions are much fewer than those of crystalline materials. Another serious problem is that the existing datasets of multiple properties for amorphous alloys are significantly imbalanced, posing a greater challenge for multi-objective design of amorphous alloys.

To address these challenges, we developed a generative multi-task deep learning (GMTDL) framework by integrating a multi-task Wasserstein autoencoder (MTWAE) and the non-dominated sorting genetic algorithm III (NSGA-III), achieving efficient multi-objective inverse design of high-performance Fe-based amorphous alloys. Our framework effectively mitigates the challenges associated with limited and imbalanced data by leveraging shared information across multiple related properties, significantly outperforming conventional single-task models in prediction accuracy. The validity and reliability of the framework are rigorously examined and benchmarked against recently reported Fe-based alloys that are not included in the datasets. Furthermore, by employing SHapley Additive exPlanations (SHAP) and statistical analysis, we provide a comprehensive understanding of the intricate effects and synergistic interactions of key elements on soft magnetic properties and GFA. Optimal content windows of these elements are also revealed for practical guidance in materials design. Finally, we developed an online platform for the GMTDL framework to achieve convenient and efficient material design.

2. Methods

2.1. Generative multi-task deep learning framework

Figure 1 illustrates the GMTDL framework, which integrates the MTWAE[31] and the non-dominated sorting genetic algorithm III (NSGA-III).[32] Here, the MTWAE model, combining the distribution-matching capability of WAE with multi-task learning, maps alloy compositions to a latent space and captures the nonlinear relationship between compositions and multiple properties, thereby enabling simultaneous optimization of multiple material properties. The NSGA-III-based evolutionary algorithm can efficiently explore the latent space to identify alloy compositions with novel combinations of multiple properties. Thus, the GMTDL framework fully leverages the advantages of the WAE-based generative model and multi-objective optimization algorithm to achieve efficient optimization and regulation of Fe-based alloys with multiple desired properties, i.e., high saturation magnetic flux density (B_s), low coercivity (H_c), and good GFA.

2.2. Data collection and processing

We constructed datasets for three properties of Fe-based metallic glasses (MGs), i.e., saturation magnetic flux density B_s of 574 compositions, coercivity H_c of 383 compositions, and critical casting diameter D_c of 311 compositions (see Fig. 1(a)). All data were rigorously collected from peer-reviewed experimental measurements (see supplementary Tables S1–S3). Among the MG compositions in these datasets, 30 elements are involved (see supplementary Fig. S1). To input the elemental composition of each alloy into the multi-task learning model, a composition descriptor is constructed as a 30-dimensional vector of $\boldsymbol{X} = [x_1, x_2, \ldots, x_{30}]^{\mathrm{T}}$ based on the

molar ratios of 30 elements in an alloy, subject to the constraint of $\sum_{i=1}^{30} x_i = 1$. Here, x_i denotes the molar ratio of element i in an alloy. If an alloy does not contain element i, $x_i = 0$ (see supplementary materials I for more details of data processing).

Considering that the different units and numerical scales among the datasets of B_s, H_c, and D_c may result in large gradient gaps among different tasks, we standardized the raw datasets for easier model training. Note that the raw experimental datasets should be standardized through a linear transformation to guarantee that their distribution shapes are not changed. Here, Z-score transformation $\hat{y}_i^{\exp} = \left(y_i^{\exp} - \bar{y}^{\exp}\right)/\sigma$ was employed, which transforms raw data distributions into distributions with a mean of 0 and a standard deviation of 1. Here, $\hat{y}_i^{\exp}$ represents the transformed property values and $y_i^{\exp}$ refers to the original values, while $\bar{y}^{\exp}$ and σ are the average value and standard deviation of a dataset, respectively. Note that $\bar{y}^{\exp}$ and σ must be calculated from the training datasets, and these two parameters are then used for transforming the test datasets. In our work, the B_s, H_c, and D_c datasets were randomly divided into two subsets: 80% for training and 20% for testing.

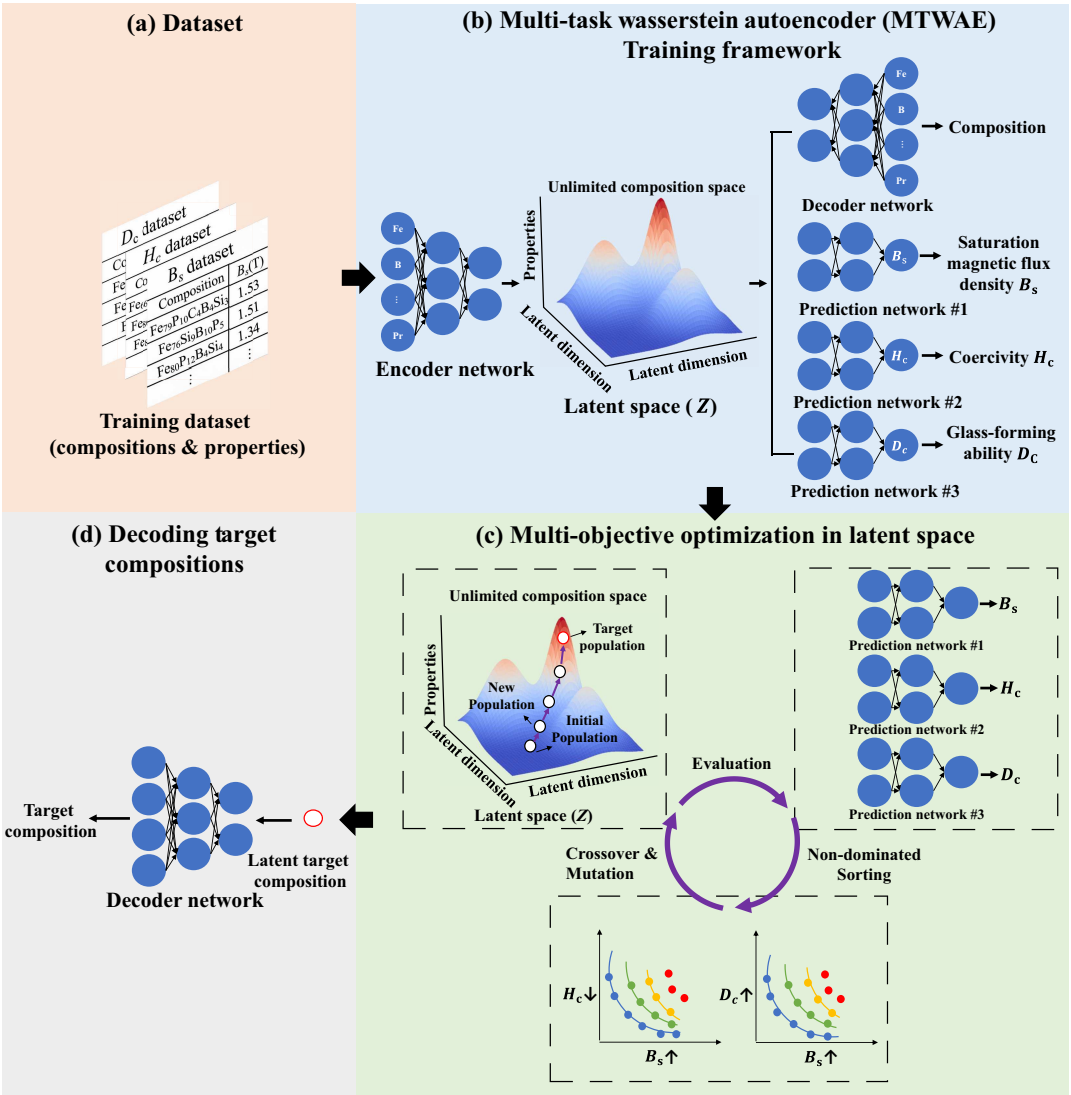


Fig. 1. Schematic of the generative multi-task deep learning framework. (a) Dataset acquisition of alloy compositions and properties of B_s, H_c, and D_c. (b) The MTWAE model, which maps compositions into a latent space and simultaneously predicts properties. (c) NSGA-III, which performs multi-objective optimization in the latent space using the MTWAE predictors for evaluation and generates Pareto-optimal solutions. (d) The final optimal latent solutions are decoded back into candidate alloy compositions.

2.3. MTWAE model

To fully leverage the limited experimental data and directly generate novel alloy compositions with multiple desired properties, we developed the MTWAE model by extending the standard WAE model to a multi-task architecture. The MTWAE model consists of five distinct neural networks: an encoder of $q_\phi(Z|X)$, a decoder of $p_\theta(\hat{X}|Z)$, and three separate predictors of $f_{\omega_p}(y_p|Z)$ for each target property y_p ($p \in \{B_s, H_c, D_c\}$). Here, Z denotes a latent space representation. ϕ, θ, and ω_p represent the parameters of the encoder network, decoder network, and predictor networks associated with property y_p, respectively. All network compo-

nents are based on multi-layer perceptrons (MLPs). Here, a softmax activation function was employed in the output layer of the decoder, which guarantees that all decoded molar fractions are non-negative and satisfy the constraint of $\sum x_i = 1$ ($i = 1, 2, \ldots, 30$) without any additional post-processing (see supplementary materials II for the detailed architecture of the MTWAE model).

The MTWAE model was trained to fit the distribution of the datasets of both alloy compositions and properties shown in Fig. 1(b). The model training is essentially an optimization of a total loss function, $L_{\text{total}} = \sum_{\text{task}} w_{\text{task}} L_{\text{task}}$, which is a sum of weighted individual task losses. Here, w_{task} denotes the weight of each task loss L_{task} for balancing its contribution to the total loss, and $L_{\text{task}} = L_{\text{recon}} + L_{\text{pro}} + L_{\text{MMD}}$. L_{recon}, L_{pro}, and L_{MMD} are reconstruction loss, prediction loss, and maximum mean discrepancy loss, respectively[33] (see supplementary materials II for details of the MTWAE model training).

To address the significant imbalance in the sizes of these datasets, we employed a dual strategy of resampling and inverse sample-size weighting. This approach effectively balances the contribution of each task during training, leading to improved overall performance (see Supplementary Figs. S3–S5). Furthermore, we optimized the latent-space dimensionality, identifying $k = 8$ as the optimal dimension that balances reconstruction fidelity and prediction accuracy (see supplementary Fig. S6). The final optimized model demonstrates strong predictive performance on the test dataset, achieving coefficients of determination $R^2 \approx 0.88$ for B_s, 0.49 for $\ln(H_c)$, and 0.63 for D_c, respectively (see supplementary Fig. S7). Note that the R^2 value for $\ln(H_c)$ is lower than those for B_s and D_c. This is mainly because coercivity is an extrinsic property and is strongly affected by microstructural features and processing conditions beyond composition. In addition, the H_c dataset is relatively smaller, providing less training information. Although incorporating processing- or microstructure-related descriptors may further improve the prediction of H_c, the acquisition of such information remains a significant challenge in this field. Nevertheless, the MTWAE model still outperforms single-task ML models in H_c prediction (see Fig. 2(f)).

2.4. Multi-objective evolutionary optimization

In the evolutionary optimization shown in Fig. 1(c), our framework employs NSGA-III to effectively maintain solution diversity and uniformly approximate complex Pareto fronts by leveraging a reference-point-based approach. In this procedure, candidate solutions in the latent space are iteratively evolved via genetic operations (selection, crossover, and mutation). Property predictions by the predictors in the MTWAE model guide the evolution toward latent representations associated with optimal combinations of multiple properties, i.e., high B_s, low H_c, and high D_c, effectively managing trade-offs among these properties. Upon reaching a predefined criterion (e.g., maximum number of generations or target property thresholds), these optimal latent representations are decoded into explicit alloy compositions by the decoder in the MTWAE model (see Fig. 1(d)). To realize efficient multi-objective evolutionary optimization, we utilized the Genetic and Evolutionary Algorithm Toolbox for Python with High Performance (GEATPy) [34] (see supplementary materials III for implementation details).

3. Results

3.1. Generative exploration and diversity analysis of generated alloy compositions

First, we evaluated the ability of the MTWAE model to generate diverse alloy compositions with multiple desired properties simultaneously, which has been argued to be a prerequisite for addressing inverse materials design tasks.[35] Here, we chose $k = 8$ as the optimal dimensionality of the latent space and trained the MTWAE model on the entire training dataset containing B_s, H_c, and D_c data. We randomly generated 3000 Fe-based alloy compositions and predicted the corresponding B_s, H_c, and D_c values using the trained MTWAE model.

Figures 2(a)–2(c) show the distributions of the B_s, $\ln(H_c)$, and D_c values for the existing and generated alloys, respectively. It is found that the property distributions of the generated alloys (blue) mostly overlap with those of the existing alloys (red). However, the density of the generated alloys with $B_s > 1.6$ T or $H_c < 1$ A/m is lower than that of the existing ones. This may be due to the random generation of alloys, which makes it difficult to search for alloys with extremely high B_s or small H_c. Among the 3000 generated alloys, 221 alloys are found to simultaneously satisfy the criteria of $B_s > 1.5$ T, $\ln(H_c) < 1.5$ A/m, and $D_c > 1$ mm, as shown in Figs. 2(a)–2(c), and are denoted as target alloys (green). These results highlight the capability of the model to generate Fe-based MG compositions with high-performance soft magnetic properties.

To analyze the diversity of the generated alloy compositions, we reduced the high-dimensional latent space to two dimensions using the t-distributed stochastic neighbor embedding (t-SNE) method.[36] Figure 2(d) visualizes the composition distributions of the existing and generated alloys in the 2D latent space. It can be seen that the generated alloys (blue) not only cover the existing ones (red) but also extend to nearby regions. This indicates that our MTWAE model can capture the composition distribution in the training dataset and generate new alloy compositions in a reliable way. This also indicates that the alloy compositions generated by the MTWAE model are as diverse as the existing ones.

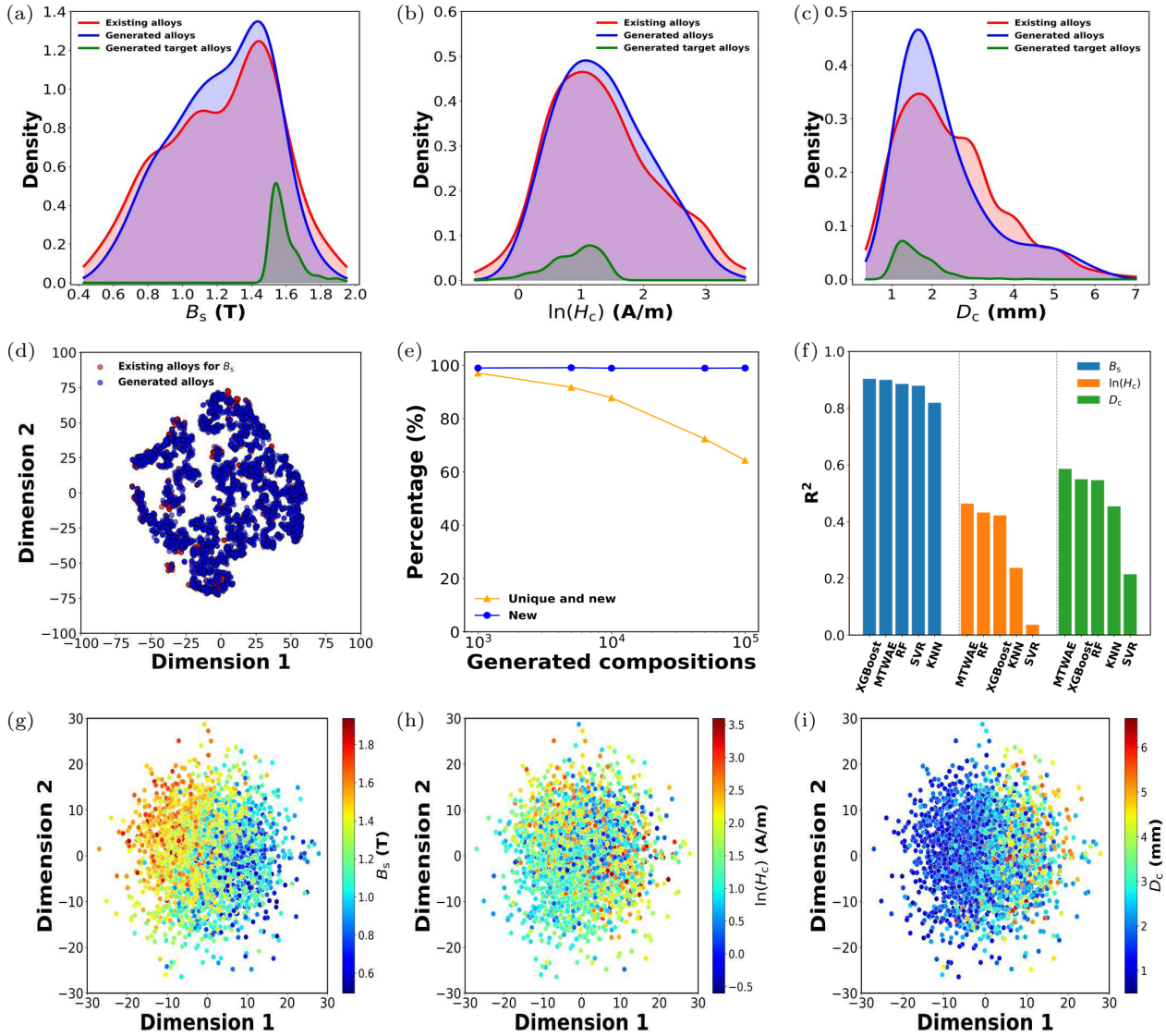


Fig. 2. Generation of diverse alloy compositions with multiple desired properties. (a)–(c) Comparison of the property distributions of existing alloys (red) and generated alloys (blue) for saturation magnetic flux density (B_s), coercivity (ln(H_c)), and critical casting diameter (D_c), respectively. The green region denotes the target alloys that simultaneously satisfy $B_s > 1.5$ T, ln(H_c) < 1.5 A/m, and $D_c > 1$ mm. (d) t-SNE visualization of the compositional distributions of existing and generated alloys. (e) Analysis of the uniqueness of the generated alloys (ranging from 1000 to 100000). (f) Comparison of the property prediction accuracy between the MTWAE model and traditional ML models (SVR, KNN, RF, XGBoost). (g)–(i) Distributions of the 3000 randomly generated compositions in the latent space colored by B_s, ln(H_c), and D_c values, respectively. Here, principal component analysis (PCA) was used to compress the 3000 generated compositions in the latent space from 8 dimensions to 2 dimensions.

Moreover, the MTWAE model can generate a substantial number of unique and new alloy compositions. Here, two alloy compositions are considered similar if they contain the same elements and the corresponding content differences are less than 1 at.%. Thus, a generated alloy composition can be regarded as unique if it is not similar to any other alloy compositions generated by the same method, and an alloy composition is considered new if it is not similar to any alloy compositions in the B_s dataset. As shown in Fig. 2(e), among 1000 generated alloy compositions, the percentage of compositions that are both unique and new is as high as 98%. This percentage still reaches 64% after 100000 alloy compositions are generated. It is also found that 99% of the generated alloy compositions are new (see Fig. 2(e)). This demonstrates that the MTWAE model can generate diverse alloy compositions without significant saturation even at a large scale, and almost all of these alloy compositions are new compared with the training dataset. These results illustrate the ability of the MTWAE model to generate unique and new alloy compositions.

Next, we demonstrated the property prediction ability of the MTWAE model by benchmarking it against several traditional ML models, such as support vector regression (SVR), K-nearest neighbors (KNN), random forest (RF), and extreme gradient boosting (XGBoost) (see supplementary Table S4 for the optimal hyperparameters of these traditional ML models). The prediction performance was systematically evaluated using 5-fold cross-validation. As shown in Fig. 2(f), the MTWAE model significantly outperforms the traditional ML

models in predicting H_c and D_c. In the B_s prediction task, its performance is comparable to that of the best-performing XGBoost model, despite the smaller weight assigned to the B_s predictor during the training of the MTWAE model (see Methods for more details). These results indicate that, through multi-task learning, the MTWAE model exploits shared knowledge from datasets across different tasks and benefits from the combined datasets, which enhances prediction accuracy and generalization capability, particularly when each dataset is quite limited.[37,38] For the traditional ML models, however, they are trained independently for each single-property prediction task and therefore fail to share knowledge across different tasks, resulting in reduced prediction accuracy and a higher risk of overfitting.[27]

Therefore, the MTWAE model couples high generative diversity with superior prediction accuracy and thus establishes a practical foundation for reliable inverse design. Next, we sought to understand how the MTWAE model captures and organizes the complex relationships between alloy compositions and multiple properties. Here, we characterized the distribution of compositions with specific properties in the latent space by employing principal component analysis (PCA)[39] to reduce the 8-dimensional latent space of the model to two dimensions. As shown in Fig. 2(g), alloy compositions with high B_s values (red dots) are mainly distributed on the left side of the latent space, while compositions with low B_s values (blue dots) are located on the right side. This indicates that the MTWAE model can effectively organize alloy compositions in the latent space according to B_s properties. Different from the distribution of B_s, compositions with high D_c values are located on the right side of the latent space, whereas those with low values are on the left side, as shown in Fig. 2(i). The difference in the distributions of B_s and D_c in the latent space indicates that the model successfully captures the trade-off between B_s and D_c and assigns clear regional divisions in the latent space for different properties. Notably, the distribution of alloy compositions with H_c values in the latent space shows a complex feature (see Fig. 2(h)). Compositions with high H_c values (red dots) are located at the end of the latent space, while those with low H_c values are located in the central region, demonstrating a complex relationship between H_c and alloy compositions.

The above results reveal the significant advantages of the MTWAE model in multi-task learning: by sharing knowledge between different tasks of B_s, $\ln(H_c)$, and D_c, the MTWAE model is able to effectively represent and organize the relationships between multiple properties and alloy compositions in a unified latent space, which results in complementary and collaborative knowledge across tasks. In addition, the latent space unifying multiple properties allows exploration of the alloy composition space with multiple targeted properties more efficiently in the inverse design framework, accelerating the discovery of high-performance alloy materials.

3.2. Efficient multi-objective inverse design of Fe-based amorphous alloys

In the above section, we established a robust MTWAE model that is capable of accurately predicting B_s, H_c, and D_c while simultaneously generating corresponding alloy compositions. To realize efficient multi-objective inverse design for Fe-based MGs with high-performance soft magnetic properties, we incorporated the NSGA-III algorithm into the MTWAE model. Here, NSGA-III is used to efficiently search for latent composition representations in the latent space obtained by the MTWAE model and provide multi-objective optimization for the trade-offs between the $B_s \sim D_c$, $B_s \sim H_c$, and $H_c \sim D_c$ property pairs. In the optimization, B_s and D_c are maximized, while $\ln(H_c)$ is minimized. The searched latent composition representations are subsequently decoded into corresponding alloy compositions using the decoder in the MTWAE model. In the multi-objective optimization, a balanced set of solutions, known as Pareto optimal solutions, is identified, which provides the best possible trade-offs among multiple properties.

Figure 3(a) visualizes the Pareto optimal solutions in the diagram of B_s–$\ln(H_c)$–D_c obtained with a population size of 200 across 500 generations. While the red circles (target MGs) represent the Pareto optimal solutions that meet all the target properties of $B_s > 1.5$ T, $\ln(H_c) < 1.5$ A/m, and $D_c > 1$ mm, the gray triangles (other MGs) represent the Pareto optimal solutions that do not meet at least one target property. The green, blue, and orange circles are the projections of the Pareto optimal solutions onto the B_s–D_c, B_s–$\ln(H_c)$, and D_c–$\ln(H_c)$ plots, respectively, representing the trade-offs between each pair of properties. The data exhibit clear trends: a negative B_s–D_c relation (higher B_s typically coincides with smaller D_c) and a positive B_s–$\ln(H_c)$ relation (higher B_s accompanies higher $\ln(H_c)$). The Pareto optimal solutions are well spread, covering approximately $B_s \approx 1.5 \sim 2.0$ T, $\ln(H_c) \approx -0.5 \sim 1.5$ A/m, and $D_c \approx 2 \sim 6$ mm, with a denser cluster near $B_s \approx 1.6 \sim 1.8$ T and $\ln(H_c) \approx 0.3 \sim 1.0$ A/m. This indicates that the GMTDL framework achieves good trade-offs between the conflicting properties.

To illustrate the ability of the GMTDL framework to identify new alloy compositions with superior properties, we compared the Pareto optimal solutions (the candidate alloys) of each pair of properties with the experimental data in the datasets. As shown in Figs. 3(b)–3(d), the Pareto optimal solutions extend the feasible performance space beyond the region covered by the experimental data, demonstrating that the GMTDL framework successfully identifies new alloy compositions and significantly pushes the achievable performance

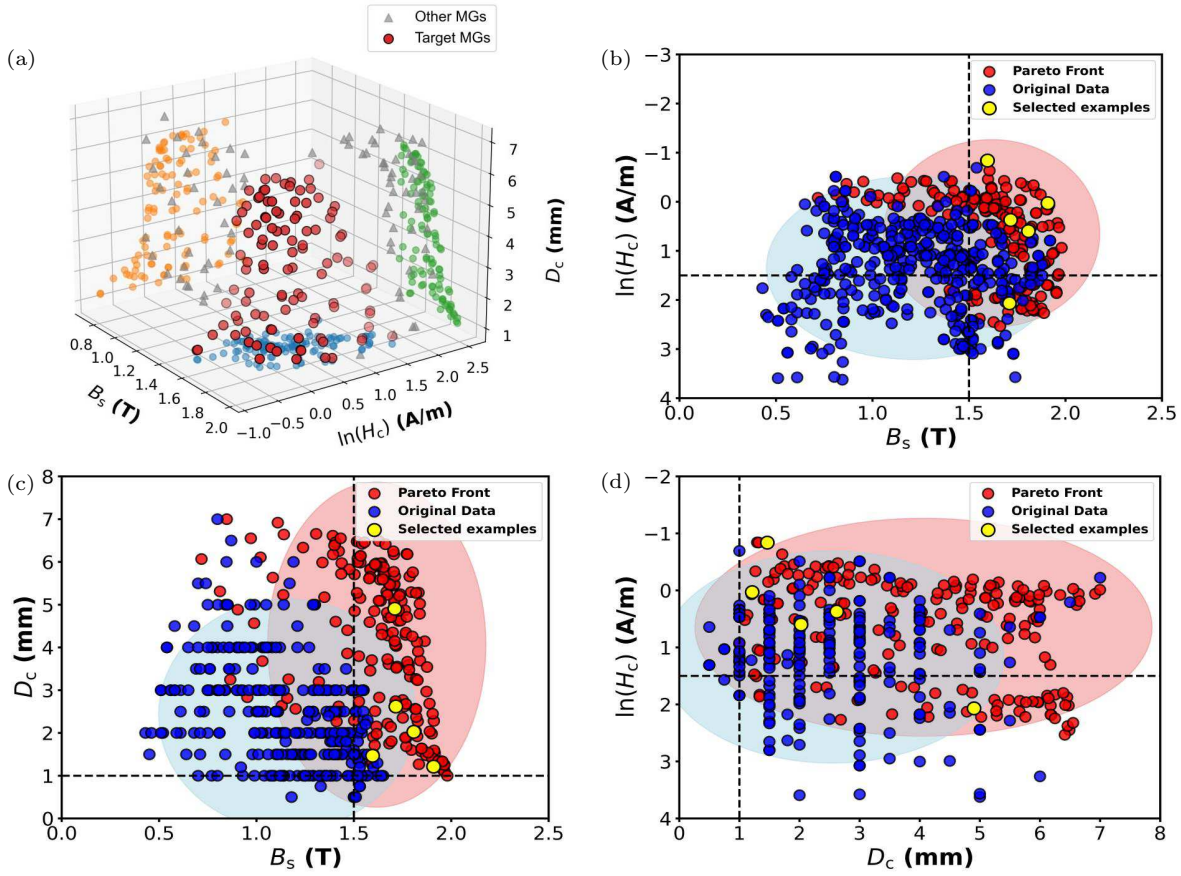


Fig. 3. Multi-objective optimization of alloy properties. (a) Visualization of Pareto-optimal solutions obtained by the GMTDL framework in the three-dimensional property space of saturation magnetic flux density (B_s), coercivity (ln(H_c)), and critical casting diameter (D_c). Red circles denote solutions simultaneously meeting the target criteria ($B_s > 1.5$ T, ln(H_c) < 1.5 A/m, $D_c > 1$ mm), while gray triangles represent non-ideal solutions. Green, blue, and orange circles indicate the projections of target solutions onto the $B_s \sim D_c$, $B_s \sim \ln(H_c)$, and $D_c \sim \ln(H_c)$ performance planes, respectively. (b)–(d) Comparison between the Pareto front obtained by the GMTDL optimization and experimental data on pairwise property planes ($B_s \sim \ln(H_c)$, $B_s \sim D_c$, and $D_c \sim \ln(H_c)$), demonstrating the framework's capability to effectively expand the experimental performance boundaries.

boundaries toward regions with better trade-offs between conflicting properties. Specifically, Fig. 3(b) showcases many candidate alloys that achieve a satisfactory trade-off between high B_s and low ln(H_c). In the experimental dataset, however, alloys with high B_s (> 1.5 T) are typically accompanied by higher ln(H_c) (> 1.5 A/m). The trade-offs of $B_s \sim D_c$ and $D_c \sim H_c$ also show similar trends (see Figs. 3(c) and 3(d)). Therefore, our GMTDL framework successfully identifies new alloy compositions with superior properties.

3.3. Model validation and discovery of high-performance Fe-based amorphous alloys

In this section, we rigorously validated our MTWAE model and assessed its generalizability and predictive power from two aspects. One is that we applied our MTWAE model to predict the B_s values of given Fe-based amorphous alloys. To demonstrate this, we applied the MTWAE model to 12 Fe-based alloys reported very recently that were not included in our datasets. As shown in Fig. 4(a), the MTWAE model exhibits remarkable accuracy in predicting B_s. For amorphous alloys of $Fe_{68.2}Co_{17.5}B_{13}Si_{0.5}Cu_{0.8}$ and $Fe_{79.7}Co_6B_{13}Si_{0.5}Cu_{0.8}$ fabricated by Guo *et al.*,[40] the predicted B_s values by the MTWAE model are 1.92 T and 1.86 T, respectively, with MAE ≈ 0.04 T, which are very close to the experimentally measured B_s values of 1.90 T and 1.81 T. This confirms the predictive power of our model for Fe-based amorphous alloys with ultrahigh B_s.

For amorphous alloys of $Fe_{85}B_{12}Si_2V_{0.5}Cu_{0.5}$, $Fe_{76.5}Co_{8.5}B_{12}Si_2V_{0.5}Cu_{0.5}$, $Fe_{68}Co_{17}B_{12}Si_2V_{0.5}Cu_{0.5}$, and $Fe_{68.8}Co_{17.2}B_{11}Si_2V_{0.5}Cu_{0.5}$ synthesized by Li *et al.*,[16] the predicted B_s values are about $1.70 \sim 1.87$ T with MAE $\approx$ 0.10 T, which are quite close to the experimental values of $1.58 \sim 1.84$ T. Moreover, our model reproduces the variation tendency of the B_s value with Co content, which first increases and then decreases as the Co content exceeds 17%.[16] These results indicate that our MTWAE model not only accurately predicts the B_s values but also correctly captures the essential Fe–Co exchange-coupling mechanism that governs B_s.[41,42]

Our MTWAE model can also estimate the B_s values of the amorphous precursors of Fe-based amorphous/nanocrystalline alloys. Very recently, Yang *et al.*[43] developed several Fe-based amorphous/nanocrystalline alloys with B_s exceeding

1.9 T. For the amorphous precursors of these Fe-based alloys, all the predicted B_s values are larger than 1.7 T, as shown in the right panel of Fig. 4(a). It is well known that the B_s values of amorphous precursors are smaller than those of the corresponding amorphous/nanocrystalline counterparts, because the fine grains smaller than 20 nm formed within the amorphous matrix after annealing possess higher saturation magnetization than the residual amorphous matrix, thereby further enhancing the B_s values.[43]

In addition to accurately predicting the B_s of Fe-based alloys, the MTWAE model can simultaneously provide predictions for H_c and D_c (see Table 1). Note that D_c serves as an indicator of the GFA of alloys, and the predicted D_c values reflect the potential GFA of alloys but do not necessarily correspond to the actual critical diameter of a given alloy under specific experimental conditions. The distribution of experimentally measured D_c values is predominantly concentrated within the range of $1 \sim 3$ mm, and the MTWAE model predictions align closely with this distribution (see supplementary Fig. S2(c)), highlighting the remarkable reliability of the MTWAE model in predicting the GFA of Fe-based alloys. For the 12 alloy compositions listed in Table 1, the predicted D_c values primarily range from 1.12 to 1.39 mm, all exceeding 1 mm, indicative of good GFA of these alloys. Although the critical diameters of the Fe-based alloys mentioned above were not measured by copper mold casting methods in experiments, their good GFA has been confirmed by the successful fabrication of Fe-based MG ribbons using melt spinning.[16,40,43] Furthermore, the predicted H_c values are highly consistent with experimental findings; for instance, amorphous alloys prepared by Yang *et al.*[43] typically exhibit coercivities above 10 A/m in their amorphous state, and correspondingly, the MTWAE model also predicts similar H_c values for nearly all these alloys, confirming the accuracy of the MTWAE model in predicting coercivity for amorphous alloys.

The other aspect is that our GMTDL framework can navigate the search in the vast compositional space to identify high-performance Fe-based amorphous alloys. With a population size of 500 after 1000 generations, the GMTDL framework pinpoints a Pareto front of 95 optimal compositions that simultaneously satisfy the more stringent criteria, i.e., $B_s > 1.75$ T, $\ln(H_c) < 1.5$ A/m, and $D_c > 1.0$ mm. Some compositions with ultra-high B_s, ultra-low H_c, and good GFA are listed in Table 1 (see supplementary Table S5 for all predicted compositions). These newly discovered candidates exhibit much superior properties, located in a high-performance region of the property space that is sparsely populated by both alloys in the datasets (gray squares) and recently reported high-performance alloys (blue triangles) (see Figs. 4(b)–4(d) and supplementary Table S5). For instance, Fig. 4(b) reveals that most of these compositions exhibit substantially low H_c ($\ln(H_c) < 1.5$ A/m) while maintaining high B_s (> 1.75 T). Moreover, these candidate alloys also tend to possess larger D_c than those in the dataset and recently reported Fe-based alloys, while retaining high B_s, as shown in Fig. 4(c). In addition, the newly discovered compositions simultaneously achieve both high D_c and low $\ln(H_c)$, as shown in Fig. 4(d).

Table 1. Fe-based alloy compositions with experimentally measured and predicted saturation magnetic flux density (B_s), predicted coercivity (H_c), and critical casting diameter (D_c) values. Compositions 1–6 are Fe-based amorphous alloys, whereas compositions 7–12 are Fe-based amorphous/nanocrystalline alloys. All compositions 1–12 were experimentally fabricated very recently. Compositions 13–20 are predicted Fe-based amorphous alloys with ultra-high B_s and ultra-low H_c generated by our model.

	Fe-based alloy compositions	Experimental B_s (T)	Predicted B_s (T)	Predicted $\ln(H_c)/H_c$ (A/m)	Predicted D_c (mm)
1	$Fe_{68.2}Co_{17.5}B_{13}Si_{0.5}Cu_{0.8}$[40]	1.90	1.92	1.19/3.29	1.23
2	$Fe_{79.7}Co_{6}B_{13}Si_{0.5}Cu_{0.8}$[40]	1.81	1.86	1.25/3.51	1.39
3	$Fe_{85}B_{12}Si_{2}V_{0.5}Cu_{0.5}$[16]	1.58	1.70	2.57/13.07	1.31
4	$Fe_{76.5}Co_{8.5}B_{12}Si_{2}V_{0.5}Cu_{0.5}$[16]	1.65	1.80	2.09/8.08	1.17
5	$Fe_{68}Co_{17}B_{12}Si_{2}V_{0.5}Cu_{0.5}$[16]	1.84	1.87	1.79/6.03	1.38
6	$Fe_{68.8}Co_{17.2}B_{11}Si_{2}V_{0.5}Cu_{0.5}$[16]	1.72	1.83	2.45/11.59	1.32
7	$Fe_{70.11}Co_{15.39}Ni_{1.5}B_{9}P_{3}C_{1}$[43]	1.92	1.76	3.32/27.66	1.38
8	$Fe_{69}Co_{16}Ni_{1}Si_{3}B_{11}$[43]	1.92	1.72	2.08/8.00	1.12
9	$Fe_{64.13}Co_{21.38}Ni_{1.5}B_{8.5}P_{3}C_{1}V_{0.5}$[43]	1.90	1.74	2.80/16.44	1.28
10	$Fe_{68.4}Co_{17.1}Ni_{1.5}B_{9}P_{3}C_{1}$[43]	1.90	1.75	3.36/28.79	1.37
11	$Fe_{64.13}Co_{21.38}Ni_{1.5}B_{8.5}P_{3}C_{1}Mo_{0.5}$[43]	1.87	1.74	2.81/16.77	1.29
12	$Fe_{64.13}Co_{21.38}Ni_{1.5}B_{9}P_{3}C_{1}$[43]	1.85	1.75	2.86/17.51	1.31
13	$Fe_{78.57}Co_{7.49}B_{12.15}Si_{1.55}Cu_{0.11}$	–	1.91	0.48	1.48
14	$Fe_{73.24}Co_{14.13}B_{11.29}Si_{1.18}$	–	1.96	0.74	1.27
15	$Fe_{71.26}Co_{15.98}B_{11.35}Si_{1.22}Nb_{0.10}$	–	1.95	0.70	1.34
16	$Fe_{65.76}Co_{19.43}B_{13.43}Si_{0.95}Nb_{0.33}$	–	1.98	0.75	1.13
17	$Fe_{40.20}Co_{38.42}B_{19.75}Si_{0.19}Nb_{0.95}Y_{0.27}$	–	1.93	0.19	1.42
18	$Fe_{67.99}Co_{0.29}B_{22.41}Si_{5.71}Nb_{1.35}Ni_{1.81}Cu_{0.13}Hf_{0.21}$	–	1.89	1.08	2.17
19	$Fe_{83.61}B_{14.26}Si_{0.17}P_{0.15}Nb_{0.31}Ni_{1.19}Hf_{0.14}$	–	1.87	1.43	2.60
20	$Fe_{63.27}Co_{2.23}B_{21.01}Si_{8.17}Nb_{4.73}Ni_{0.32}Cu_{0.14}$	–	1.85	0.98	2.45

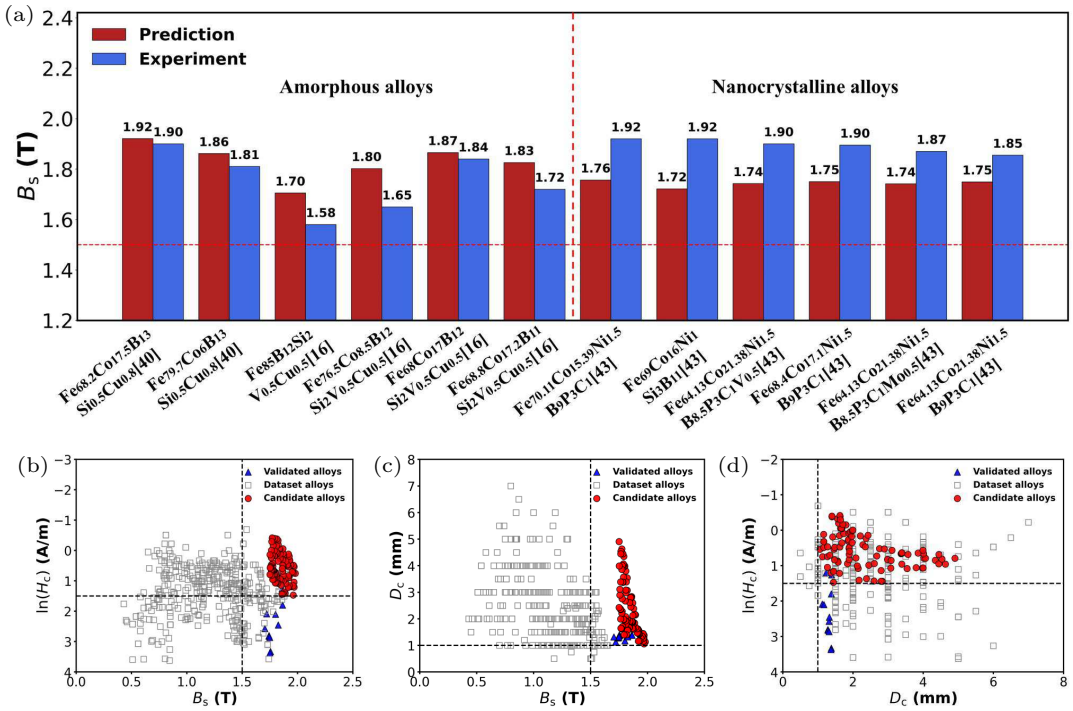


Fig. 4. Validation of the MTWAE model and discovery of high-performance Fe-based amorphous alloys. (a) Comparison between MTWAE-predicted and experimentally measured saturation magnetic flux density (B_s) for twelve recently reported Fe-based amorphous or amorphous/nanocrystalline alloys that were not included in the training set. Two-dimensional projections of the Pareto front obtained by performing NSGA-III optimization for 1000 generations with a population size of 500 latent vectors in the MTWAE latent space: (b) $B_s \sim \ln(H_c)$; (c) $B_s \sim D_c$; (d) $D_c \sim \ln(H_c)$. Red circles indicate 95 newly discovered alloy compositions simultaneously satisfying $B_s > 1.75$ T, $\ln(H_c) < 1.5$ A/m, and $D_c > 1.0$ mm; squares represent experimental samples from the training dataset; triangles denote the literature alloys shown in panel (a).

To go beyond the property-space validation and the discovery of superior alloy compositions, and to assess whether the discovered candidates remain within empirically plausible thermodynamic–structural regimes, we further conducted a physics-guided plausibility check by projecting alloys in the datasets and the GMTDL candidates (see supplementary Table S5) onto physically motivated descriptor planes. Here, three physical descriptors were considered, i.e., atomic-size mismatch δ, mixing enthalpy ΔH_{mix}, and a theoretical saturation magnetic flux density B_s^{cal} (see supplementary materials IV for definitions). While δ and ΔH_{mix} are related to the GFA,[44] B_s^{cal} corresponds to B_s.[45] To visualize the distribution, we plotted the δ–ΔH_{mix} map together with two magnetism-related projections, i.e., B_s^{cal}–δ and B_s^{cal}–ΔH_{mix}. As shown in Fig. 5(a), the dataset-defined high-performance subsets occupy a compact region characterized by moderate δ and negative ΔH_{mix}. Moreover, the GMTDL candidates largely fall within or in proximity to the envelope spanned by these experimentally observed subsets. No obvious drift toward extreme outliers is observed in the composition–thermodynamics descriptor space. In addition, Figs. 5(b) and 5(c) indicate that the candidates preferentially populate the upper envelope of B_s^{cal}, consistent with the design objective of achieving higher predicted B_s (e.g., the more stringent target $B_s > 1.75$ T used to define the highlighted candidates in Fig. 5). Moreover, Fig. 5(c) suggests a mild shift of candidates toward less negative ΔH_{mix} along the high-B_s^{cal} ridge, which is consistent with the commonly observed trade-off between enhancing saturation performance and maintaining strongly negative mixing enthalpy that favors glass formation of Fe-based alloys.

To further substantiate the validity of the GMTDL framework, we compared the predicted candidates (see supplementary Table S5) with recently reported Fe-based alloys with high B_s values (see Table 1). The GMTDL framework autonomously converges to compositions that are close to the experimental exemplars in both composition and properties. For instance, the candidate of $Fe_{68.47}B_{13.11}Si_{1.20}Co_{17.03}$ closely matches the reported alloy of $Fe_{68.2}B_{13}Si_{0.5}Co_{17.5}Cu_{0.8}$ in composition, with nearly identical total magnetic-element content, i.e., 85.50 vs. 85.70 at.% of Fe + Co, and exhibits comparable B_s values (1.97 vs. 1.90 T). Likewise, compared to the reported $Fe_{68}Co_{17}B_{12}Si_2V_{0.5}Cu_{0.5}$ alloy, the candidate $Fe_{67.13}Co_{17.44}B_{12.79}Si_{2.09}Nb_{0.43}$ alloy has a highly similar magnetic-element content (84.57 vs. 85.00 at.%) and B_s values (1.94 T vs. 1.84 T), indicating that the framework rediscovers the same high-performance regions in composition space. These quantitative matches across composition, total magnetic-element content, and B_s values provide firm evidence that the GMTDL framework can learn the governing composition–property relationship and reliably rediscover the experimentally validated regions of Fe-based alloys with ultra-high B_s. Thus, the framework generates large pools of reliable, high-performance alloy candidates, markedly reducing

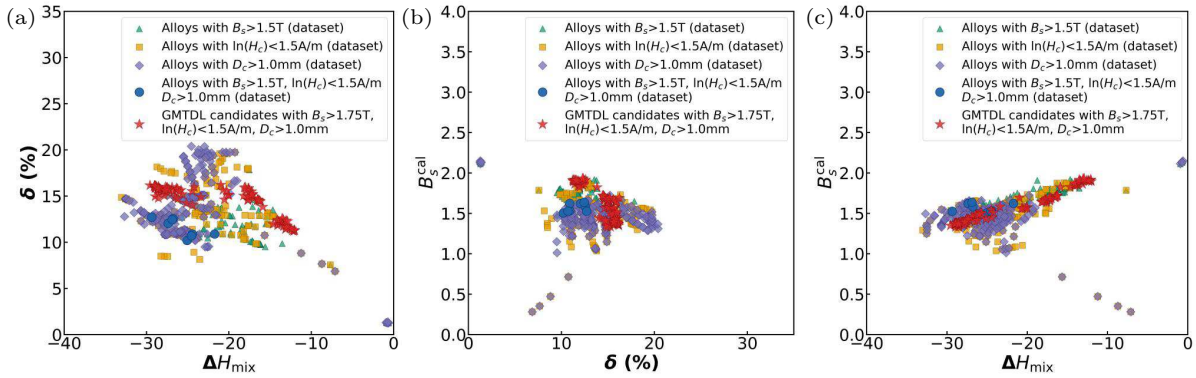


Fig. 5. Physics-guided descriptor mapping of GMTDL-discovered Fe-based amorphous-alloy candidates. Projections of alloys in the datasets and GMTDL candidates onto the physically motivated descriptor planes of $\delta \sim \Delta H_{\mathrm{mix}}$ (a), $B_{\mathrm{s}}^{\mathrm{cal}} \sim \delta$ (b), and $B_{\mathrm{s}}^{\mathrm{cal}} \sim \Delta H_{\mathrm{mix}}$ (c), respectively. Here, δ denotes the atomic-size mismatch, ΔH_{mix} denotes the mixing enthalpy, and $B_{\mathrm{s}}^{\mathrm{cal}}$ denotes the composition-only theoretical saturation-moment proxy, respectively. Green triangles denote alloys with $B_{\mathrm{s}} > 1.5$ T in the dataset, orange squares denote alloys with $\ln(H_{\mathrm{c}}) < 1.5$ A/m in the dataset, and purple diamonds denote alloys with $D_{\mathrm{c}} > 1.0$ mm in the dataset. Blue circles indicate alloys that satisfy all three criteria simultaneously ($B_{\mathrm{s}} > 1.5$ T, $\ln(H_{\mathrm{c}}) < 1.5$ A/m, and $D_{\mathrm{c}} > 1.0$ mm) in the dataset. Red stars represent GMTDL candidates meeting more stringent design targets based on GMTDL predictions, i.e., $B_{\mathrm{s}} > 1.75$ T, $\ln(H_{\mathrm{c}}) < 1.5$ A/m, and $D_{\mathrm{c}} > 1.0$ mm.

experimental trial-and-error and accelerating the discovery of next-generation soft magnetic materials. Note that alloys numbered 13–20 in Table 1, as well as those in supplementary Table S5, are predicted by the GMTDL framework and have not yet been experimentally tested.

4. Discussion

4.1. Comparison with previous ML-based Strategies

To demonstrate the search efficiency of our GMTDL framework for discovering compositions with target properties, i.e., $B_{\mathrm{s}} > 1.5$ T, $\ln(H_{\mathrm{c}}) < 1.5$ A/m, and $D_{\mathrm{c}} > 1$ mm, we conducted a comprehensive comparison with previous ML approaches for alloy design. Data-driven generative ML models represent one prominent approach.[46–48] While generative models alone can effectively capture data distributions, they often face great challenges in optimizing target properties.[48] ML models combined with genetic algorithms (GA + ML) constitute another approach,[49–51] which has received increasing attention. Here, we compared the GA+ML approach with our GMTDL framework using the same datasets, target criteria, NSGA-III settings, and computing platform. We implemented the GA+ML approach using the NSGA-III algorithm. In this approach, a composition space needs to be defined. Here, a composition space containing the six most prevalent elements Fe, B, Si, C, P, and Co was considered, yielding 26 alloy systems ranging from ternary to 6-element compositions. Moreover, property predictions were performed using XGBoost for B_{s} and D_{c}, and random forest for H_{c}. With population sizes of 500 over 1000 generations per alloy system, the GA + ML approach generated 13000 samples in total, of which 3428 (26%) satisfied the performance criteria, as shown in Fig. 6(a). The average values are $B_{\mathrm{s}} \approx 1.62$ T, $\ln(H_{\mathrm{c}}) \approx 1.05$ A/m, and $D_{\mathrm{c}} \approx 2.37$ mm, respectively (see Fig. 6(b)).

For the GMTDL framework, we trained ten MTWAE models with different parameter initializations to ensure robust statistical sampling. Each model was executed with a population size of 500 over 1000 generations, generating 5000 alloy compositions in total. Remarkably, 2255 candidates (45%) satisfy the predefined criteria (see Fig. 6(a)), representing a dramatic improvement over the sub-1% success rate of standalone generative models.[48] The GMTDL-generated samples exhibit superior average properties of $B_{\mathrm{s}} \approx 1.65$ T, $\ln(H_{\mathrm{c}}) \approx 0.19$ A/m, and $D_{\mathrm{c}} \approx 3.05$ mm (see Fig. 6(b)). These metrics substantially exceed the target thresholds, with B_{s} surpassing the requirement by 10%, $\ln(H_{\mathrm{c}})$ achieving an 87% improvement below the threshold, and D_{c} tripling the minimum requirement.

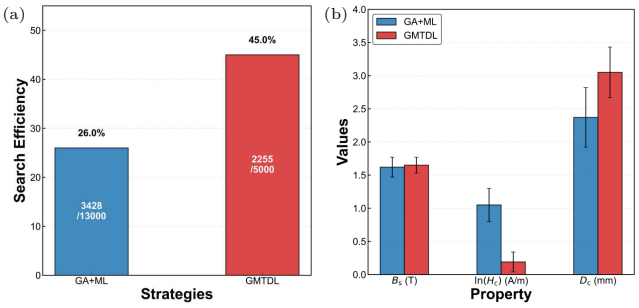


Fig. 6. Comparison of optimization strategies for alloy design. (a) Search efficiency of the GA + ML strategy and the GMTDL framework, showing the fraction of generated samples meeting target criteria ($B_{\mathrm{s}} > 1.5$ T, $\ln(H_{\mathrm{c}}) < 1.5$ A/m, and $D_{\mathrm{c}} > 1$ mm). (b) Average property values of samples satisfying target criteria generated by the GA + ML strategy and the GMTDL framework, respectively, demonstrating superior performance of the GMTDL-designed alloys across all three metrics. Error bars represent standard deviation.

Apparently, the GMTDL framework exhibits significant improvement in search efficiency compared to the GA + ML approach, while delivering superior property distributions across all three metrics. This enhanced performance stems from a fundamental advantage: the GMTDL framework initiates searches from the distribution of existing samples, navi-

gating the design space proximate to this distribution. This approach generates novel yet chemically plausible designs while maintaining prediction reliability throughout the optimization process. In contrast, the GA + ML method often encounters significant discrepancies between randomly generated samples and training data, undermining prediction reliability.[52] On the other hand, a representative GMTDL optimization run needs about 4.0 s, whereas the GA + ML approach costs about 12.7–16.8 s per alloy system, with an average time of 14.7 s. Moreover, GA + ML must optimize 26 predefined alloy systems separately, and its cumulative search time was about 383 s in our implementation. In contrast, GMTDL performs the search directly in a fixed 8-dimensional latent space and then decodes latent vectors into alloy compositions, leading to substantially lower search costs. Therefore, the GMTDL framework substantially outperforms traditional ML approaches in both efficiency and scalability for the inverse design of high-performance alloys.

4.2. Evolution of the Pareto front in the GMTDL framework

To understand why the GMTDL framework can provide accurate and efficient prediction of high-performance Fe-based soft magnetic alloys, we tracked and visualized the evolution of the composition population across multiple generations during the evolutionary optimization procedure. We initialized the population with 200 individuals and examined 0, 10, and 200 generations, respectively. In Figs. 7(a)–7(c), the t-SNE embeddings depict 3000 randomly generated compositions (blue heatmap) superimposed with Pareto optimal solutions (yellow points). These panels illustrate how the Pareto solutions transform from a random distribution in the initial generation (see Fig. 7(a)) to a more refined, higher-performance region of the design space after 200 generations (see Fig. 7(c)). Specifically, in generation 0, the randomly sampled latent variables yield a population with sparse Pareto optimal solutions, corresponding to a nearly random composition distribution. Only a small subset of these individuals achieve desirable trade-offs among B_s, H_c, and D_c. In generation 10 shown in Fig. 7(b), the Pareto solutions begin to grow, reflecting the initial success in balancing the competing objectives and indicating that the algorithm is effectively exploring the latent space. In generation 200 shown in Fig. 7(c), the Pareto-front solutions clearly separate from the main density cloud, converging toward less-populated regions that are less likely to arise from random sampling alone. This demonstrates the transformation from near-random exploration to targeted optimization, highlighting the capability of the GMTDL framework to uncover compositions with superior properties.

In addition, Figs. 7(d)–7(f) compare the pairwise properties of $B_s \sim \ln(H_c)$, $B_s \sim D_c$, and $D_c \sim \ln(H_c)$ across generations 0, 10, and 200, clearly showing how the Pareto-front solutions shift toward improved B_s, reduced $\ln(H_c)$, and enhanced D_c during the evolutionary process. These shifts confirm that the GMTDL framework successfully discovers compositions with balanced trade-offs among multiple properties. Consequently, the optimization process evolves from random sampling to a systematic, iterative search in regions of the composition space containing superior multi-objective solutions. Such results further validate the efficiency and advantage of the GMTDL framework in identifying target compositions within a vast composition space.

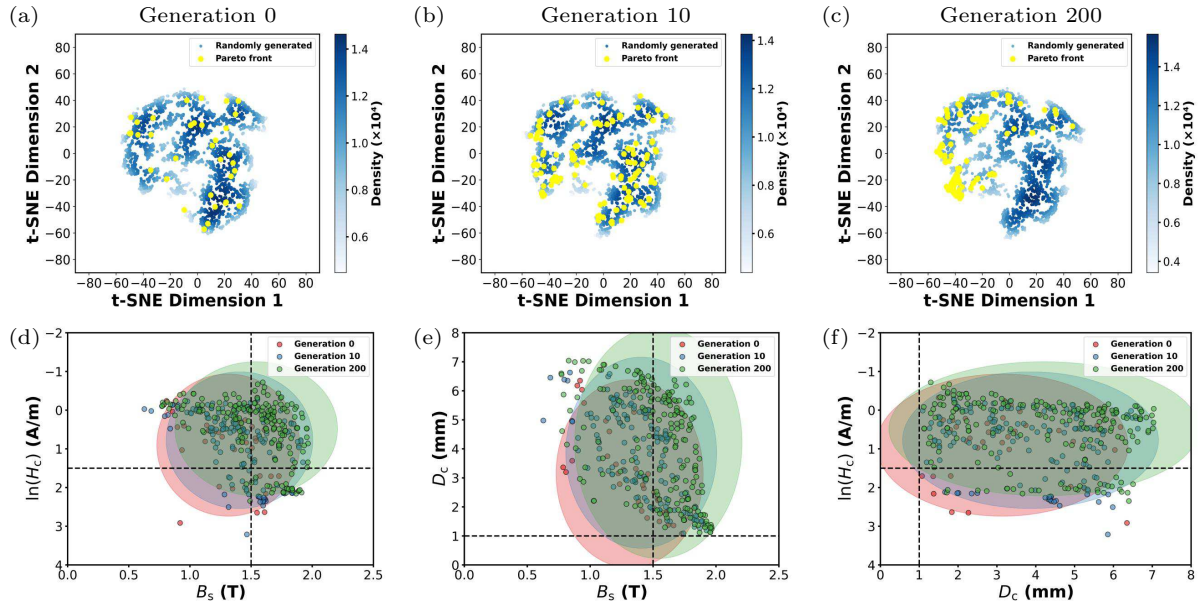


Fig. 7. Evolution of the Pareto front in the GMTDL framework. (a) t-SNE representation of the 0th-generation (initial) Pareto front, highlighting the random distribution of the initial population. (b) t-SNE representation of the 10th-generation Pareto front, showing the early progress of optimization. (c) t-SNE representation of the 200th-generation Pareto front, demonstrating refined exploration of the design space. (d)–(f) Pairwise comparisons of $B_s \sim \ln(H_c)$ (d), $B_s \sim D_c$ (e), and $D_c \sim \ln(H_c)$ (f), revealing how the solutions are progressively improved over iterations.

We also evaluated whether the high-performance solutions collapse to a single local minimum or instead arise from multiple compositionally distinct regions of the composition space by comparing representative candidates (yellow circles in Figs. 3(b)–3(d)). Although several alloys achieve the target properties, i.e., $B_s > 1.5$ T, $\ln(H_c) < 1.5$ A/m, and $D_c > 1$ mm, their chemistries differ markedly, indicating that they do not originate from the same local regions. For example, $Fe_{61.35}B_{23.38}Si_{1.00}Co_{8.98}Nb_{4.94}Y_{0.15}$ and $Fe_{72.28}B_{15.79}Si_{4.24}Co_{3.59}Nb_{1.90}Cu_{2.01}$ differ markedly in the contents of Fe and B, while $Fe_{67.95}B_{21.62}Si_{1.19}Co_{7.58}Nb_{1.48}$ and $Fe_{77.13}B_{13.45}Si_{7.53}P_{0.19}Nb_{0.22}Zr_{1.21}Ga_{0.11}$ also exhibit significant differences in the contents of Fe, B, and Co. To more clearly visualize the inherent compositional diversity of these candidate alloys, we plotted their compositions in a ternary Fe–B–Si diagram by focusing exclusively on three dominant alloying elements (see supplementary Fig. S8). Despite containing additional alloying elements, this representation effectively highlights the broad compositional distribution of the candidate alloys. This demonstrates that our multi-objective design framework can discover a diverse range of novel candidate alloys.

Note that the present GMTDL framework is established on available literature datasets and evaluates candidates mainly through learned composition–property relationships. Consequently, possible effects associated with real processing conditions, such as composition deviation, cooling-rate variation, and microstructural heterogeneity, have not yet been considered in the current study. Nevertheless, the close compositional and property-level agreement between the predicted candidates and recently reported high-performance alloys (Table 1, entries 1–12), together with the physics-guided plausibility analysis (Fig. 5), provides preliminary evidence supporting the reliability of these predictions.

4.3. Elemental design principles for high-performance Fe-based amorphous alloys

Based on the GMTDL framework, we utilized the Shapley Additive Explanations (SHAP) method[53] to provide quantitative insights into the contributions of individual elements to the predicted outcomes. We first focused on the experimental datasets and applied the SHAP method to scrutinize the influence of individual elements on B_s, H_c, and D_c. Figures 8(a)–8(c) present the SHAP plots for the 12 most prevalent elements: Fe, B, Si, P, C, Co, Nb, Ni, Mo, Zr, Ga, and Al, where positive/negative values indicate positive/negative impacts on the predicted properties. The analysis reveals a clear hierarchy of elemental influences on properties. Apparently, magnetic elements (Fe, Co) predominantly control B_s, showing strong positive SHAP values and validating that an increase in magnetic element content is the most straightforward way to enhance the saturation magnetization.[54] However, excessive Fe content may deteriorate the GFA, as the SHAP values are negative for D_c. B exhibits not only a significantly positive impact on D_c (enhancing GFA), but also largely negative SHAP values for H_c (reducing coercivity), making it crucial for both structural stability and magnetic softness.[10] Diffusion-inhibiting elements (Zr, Nb, Mo) with large atomic radii effectively enhance the GFA, but exhibit strong detrimental effects on B_s at high concentrations, necessitating precise compositional tuning.[11]

To translate these global trends into practical alloy design strategies, we systematically analyzed the SHAP-derived dependence on the contents of some key elements (see supplementary Figs. S9–S11). For Fe, the SHAP values of B_s increase almost linearly with increasing Fe content, clearly illustrating the contribution of Fe content to B_s (see Fig. S9a). The SHAP values remain positive for Fe > 72 at.%, indicating a positive contribution of Fe content to B_s, whereas the values are all negative for Fe < 65 at.%, indicating a negative contribution to B_s. On the contrary, the SHAP values of D_c continuously decrease with increasing Fe content and change from positive to negative at around 70 at.% (see Fig. S9c). This confirms the trade-off between B_s and D_c. Moreover, the SHAP values of B_s and D_c as a function of Fe content suggest an optimal Fe content window, i.e., $70 \sim 72$ at.%, to balance B_s and D_c. As the Fe content exceeds 72 at.%, its effect on D_c becomes consistently negative, indicating that additional elements are required to improve the GFA of Fe-based alloys with Fe > 72 at.%. For H_c, the SHAP values fluctuate between positive and negative over the whole Fe content range (see Fig. S9b), indicating a relatively random effect on H_c. In contrast to Fe, Co provides positive contributions to B_s when its content exceeds 5 at.% (see Fig. S9d), while exerting a random contribution to D_c (see Fig. S9f). In addition, Co may concurrently decrease H_c (negative SHAP values, Fig. S9e). This demonstrates that Co addition (> 5 at.%) may improve both B_s and H_c without deteriorating the GFA, and may even enhance the GFA. For the magnetic element Ni, it exhibits unique dual functionalities with a critical transition at 8 at.%, above which Ni simultaneously enhances B_s (see Fig. S9g, with positive SHAP values up to 0.4 T) and reduces H_c (see Fig. S9h, with negative SHAP values reaching -1.0 A/m). However, Ni has a negative impact on GFA when its content is larger than 14 at.% (see Fig. S9i), suggesting an optimal regime of 8–14 at.% for enhancing magnetic properties while maintaining acceptable GFA.

Metalloid elements show similar impacts on these properties but with distinct optimal contents (see Fig. S10). For B, when the content is below 15 at.%, the SHAP values for B_s are mostly positive, favoring the enhancement of B_s (see Fig. S10a). For H_c, the SHAP values are mostly positive be-

low 15 at.%, but become mostly negative above 15 at.% (see Fig. S10b), which benefits the reduction of H_c. For D_c, the benefit emerges beyond $\sim$ 6 at.% and strengthens with increasing content, as the SHAP values remain mostly positive (see Fig. S10c). Thus, an optimal B content window is around 15 $\sim$ 25 at.% for H_c/GFA-prioritized designs, or 10 $\sim$ 15 at.% when preserving high B_s is critical. The effect of P on B_s is quite similar to that of B, but the critical content is around 6 at.%, beyond which the SHAP values for B_s become negative, leading to reduced B_s (see Fig. S10d). However, the SHAP values for D_c remain near zero below 4 at.%, but become strongly positive above 4 at.% (see Fig. S10f), strongly favoring GFA. This confirms the role of P as an effective GFA enhancer. In contrast to B, P exhibits an almost random impact on H_c (see Fig. S10e). Thus, for P, a content range of 4 $\sim$ 6 at.% may be optimal for tuning magnetic performance. For Si, the SHAP values for B_s are positive only at very low contents (see Fig. S10g). However, the SHAP values for D_c are mostly positive when the content exceeds 2 at.% (see Fig. S10i). Similar to P, Si addition shows an almost random effect on H_c (see Fig. S10h). A narrow Si content range below 4 at.% remains suitable for simultaneously tuning magnetic properties and GFA (see Figs. S10g and S10i). When the C content exceeds 2 at.%, the penalty on B_s becomes notable (see Fig. S10j), whereas the benefit to H_c appears below 4 at.% (see Fig. S10k). In addition, improvements in D_c emerge when the C content is $\geq$ 4 at.% (see Fig. S10l). This suggests that 2 $\sim$ 4 at.% C is suitable for balanced optimization, whereas 4 $\sim$ 6 at.% C is preferable for GFA-prioritized compositions.

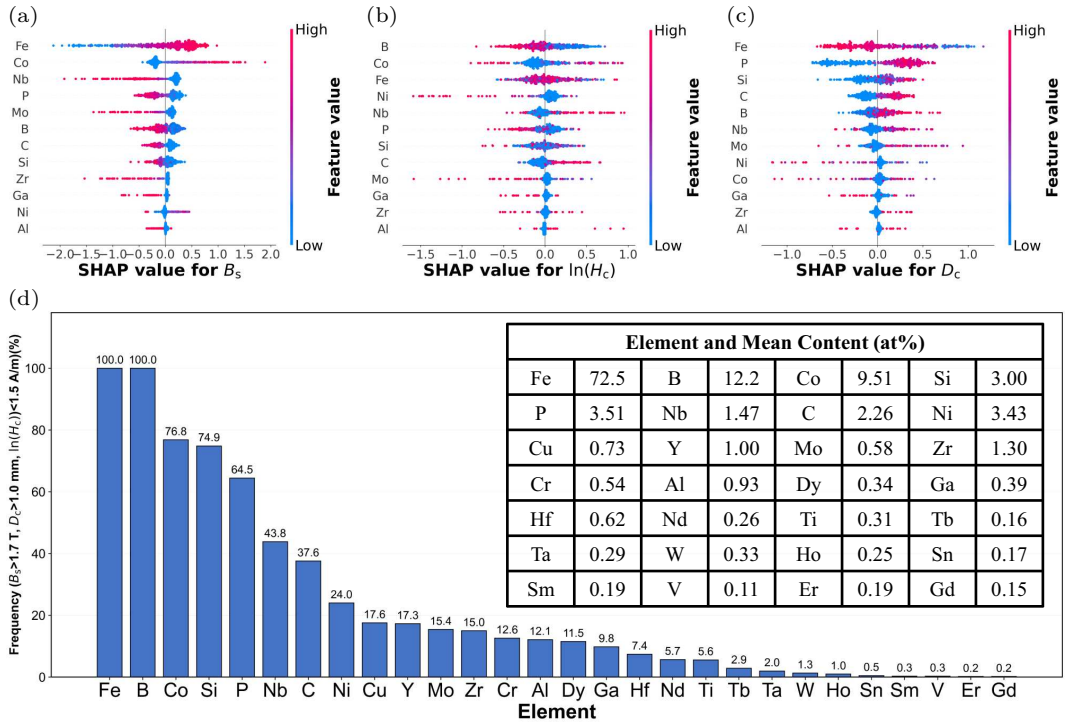


Fig. 8. Quantitative insights into element-specific contributions to the properties of Fe-based amorphous alloys via SHAP analysis and frequency statistics. SHAP values for B_s (a), H_c (b), and D_c (c). The x-axis denotes the SHAP value of each element (positive values indicate positive contributions, whereas negative values indicate negative contributions), and the y-axis ranks input features according to their importance. Each point represents an individual sample from the dataset, with the color indicating the element concentration (red represents higher concentration). (d) Statistical frequency analysis of elements within a subset of 7500 MTWAE-generated compositions with $B_s > 1.7$ T. The frequencies represent the fraction of compositions that additionally satisfy $D_c > 1$ mm and ln(H_c) < 1.5 A/m. The bar height represents the element frequency (%). The inset table shows the mean atomic concentrations (at.%) of each element.

Transition metal modifiers impose more stringent tradeoffs. Nb exhibits severe magnetic dilution — even small additions significantly weaken B_s, as indicated by SHAP values reaching -2.0 (see Fig. S11a). On the other hand, Nb can effectively reduce H_c when its content is below $\sim$ 4 at.% (see Fig. S11b), and enhances D_c above 2 at.% (see Fig. S11c). This leads to distinct optimization strategies, namely, Nb contents below 1 at.% for improving B_s, and 2 $\sim$ 4 at.% for H_c/GFA-focused designs with acceptable B_s, respectively.

Thus, the convergence of the optimal content windows for these elements — Fe (70 $\sim$ 72 at.%), Co (5 $\sim$ 10 at.%), Ni (8 $\sim$ 14 at.%), B (15 $\sim$ 25 at.%, or 10 $\sim$ 15 at.% for B_s-priority), P (4 $\sim$ 6 at.%), Si (2 $\sim$ 4 at.%), C (2 $\sim$ 4 at.% for balanced optimization or 4 $\sim$ 6 at.% for GFA-priority), and Nb ($\leq$ 1 at.% for B_s-priority or 2 $\sim$ 4 at.% for H_c/GFA-priority) — defines a highly constrained yet achievable compositional space where high B_s, low H_c, and adequate D_c for glass formation can be simultaneously realized.

Although such analyses of experimental data provide valuable insights, they are inherently limited by small sam-

ple sizes and high experimental costs. Our GMTDL framework circumvents this bottleneck by rapidly generating vast virtual libraries of alloy compositions, enabling systematic and robust statistical exploration at a scale that was previously unattainable. To elucidate the underlying elemental "design rules" governing the simultaneous optimization of high B_s, low H_c, and superior GFA, we utilized a virtual library containing 500000 alloy compositions with their predicted B_s, H_c, and D_c values, generated by ten independently trained MTWAE models. From this virtual composition library, we extracted 7500 candidates meeting stringent performance criteria ($B_s > 1.70$ T, $D_c > 1$ mm, and $\ln(H_c) < 1.5$ A/m) and calculated the occurrence frequencies and average contents for 28 elements. To validate the robustness of these findings, we generated 10000 compositions using the MTWAE model and conducted SHAP analysis, which revealed elemental trends fundamentally consistent with those identified from the experimental datasets (see supplementary Fig. S12).

Figure 8(d) shows the occurrence frequencies of the elements and their average contents among these generated alloys. It can be clearly seen that a fundamental Fe–B–Co–Si quaternary alloy system is essential for designing high-performance Fe-based alloys. The statistical results show that Fe and B are present in 100% of the retained alloys, demonstrating their indispensable roles in developing high-performance Fe-based alloys. The mean content of Fe is about 72.5 at.%, demonstrating its primary role as a magnetic contributor and fundamentally enabling high B_s. This optimal Fe content precisely aligns with that identified by the SHAP analysis (see Fig. S9a). B, with a mean content of $\sim$ 12.2 at.%, is confirmed as critical for GFA. As the lightest metalloid element, B effectively improves GFA while exhibiting the weakest dilution effect on magnetic properties among the metalloids. The prevalence of B at this concentration corresponds to the region identified in our SHAP analysis where B maintains low H_c while allowing sufficient magnetic element content for high B_s.

Co has the third-highest frequency of occurrence (76.8%), with a mean content of $\sim$ 9.5 at.%, consistent with the above SHAP analysis. According to the Slater–Pauling curve, partial substitution of Fe with Co enhances magnetic exchange interactions, leading to an increased average magnetic moment per atom.[55] Completing this core quaternary system, Si exhibits an occurrence frequency as high as 74.9%, with a mean content of $\sim$ 3.0 at.%, located within the optimal content window obtained from the SHAP analysis. While B is essential, excessive B content leads to the precipitation of Fe–B compounds during nanocrystallization, deteriorating soft magnetic properties.[56,57] Our results quantitatively validate that partial substitution of B with Si is highly effective, with Si improving the combination of GFA and magnetic softness through its intersolubility with bcc-Fe to form a bcc-(Fe,Si) phase.[58]

Apart from the primary Fe–B–Co–Si matrix, our analysis also highlights key secondary alloying elements that are critical for fine-tuning material properties. P shows the fifth-highest frequency (64.5%), demonstrating its important role in tuning the properties of Fe-based MGs. Its atomic radius (0.109 nm) is relatively larger than that of B (0.087 nm). Therefore, partial substitution of B with P may enhance exchange–coupling interactions, improving B_s.[59] Nb also plays significant roles, with a frequency of 43.8%, confirming its contribution to refining nanocrystalline grains, reducing H_c, and improving GFA despite its magnetic dilution effect.[60] C, with a frequency of 37.6%, may effectively stabilize amorphous structures.[61] Ni (24.0% frequency, $\sim$ 3.4 at.% content) serves an essential role through partial substitution for Co, effectively reducing H_c while maintaining reasonable B_s.[62]

The remarkable consistency between the SHAP analysis of experimental data and the statistical patterns in the virtual library validates the physical plausibility of the MTWAE-generated compositions and establishes quantitative, data-driven design rules for multi-objective optimization. These findings transform alloy design from empirical trial-and-error into a principled, predictive science, providing a roadmap for developing next-generation soft magnetic materials with tailored properties.

4.4. Online toolkit

To facilitate the application of the GMTDL framework, we developed an online interactive tool based on the Streamlit platform. By simply configuring parameters such as population size and the number of generations, the online toolkit provides users with an efficient and convenient way to design Fe-based alloys with desired properties for subsequent experimental preparation and synthesis. The web applications for property prediction and the GMTDL framework can be accessed at Fe-based amorphous alloys Property and GMTDL Generative Fe-based amorphous alloy Design.

5. Conclusion

In summary, we developed a generative multi-task deep learning (GMTDL) framework that enables efficient inverse design of Fe-based amorphous alloys with optimized soft magnetic properties. The framework effectively navigates the high-dimensional composition space, generating a diverse range of novel alloy candidates that push performance beyond the limits of known alloys. Moreover, the GMTDL framework overcomes the long-standing challenge of trade-offs among B_s, H_c, and GFA, and identifies high-performance alloys with all three objectives optimized simultaneously. The GMTDL

framework not only outperforms conventional ML-assisted alloy design approaches in success rate and accuracy, but also provides mechanistic insights into alloy design for guiding the development of next-generation soft magnetic alloys. Nevertheless, because H_c is highly sensitive to processing factors, such as annealing temperature, annealing time, and ribbon thickness, future improvement of the framework requires incorporating processing-related descriptors to establish a more comprehensive composition-processing-property model. In addition, the generative multi-task deep learning design strategy can be generalized to other material systems, providing a robust and intelligent tool to accelerate materials discovery for advanced technology.

Code availability

The source code for the GMTDL framework is available at GitHub. The archived version with a persistent DOI is https://doi.org/10.5281/zenodo.19272020.

Acknowledgments

Project supported by the National Natural Science Foundation of China (Grant Nos. 12574220 and 52031016). Computational resources were provided by the Physical Laboratory of High-Performance Computing at Renmin University of China.

References

[1] Silveyra J M, Ferrara E, Huber D L and Monson T C 2018 *Science* **362** eaao0195
[2] Perigo E A, Weidenfeller B, Kollar P and Fuzer J 2018 *Appl. Phys. Rev.* **5** 031301
[3] Gutfleisch O, Willard M A, Bruck E, Chen C H, Sankar S G and Liu J P 2011 *Adv. Mater.* **23** 821
[4] Shao L L, Bai R S, Wu Y X, Zhou J, Tong X, Peng H L, Liang T, Li X Z, Zeng Q S and Zhang B 2024 *Mater. Futur.* **3** 025301
[5] Herzer G 2013 *Acta Mater.* **61** 718
[6] Cullity B D and Graham C D 2008 *Introduction to Magnetic Materials* (New York: IEEE Press) pp. 439–476
[7] Kasai S, Namikawa M and Hiratani T 2016 *JFE Tech. Rep.* **21** 14
[8] Snoek J L 1948 *Physica* **14** 207
[9] Yao K F, Shi L X, Chen S Q, Shao Y, Chen N and Jia J L 2018 *Acta Phys. Sin.* **67** 016101 (in Chinese)
[10] Shi L X, Hu X Y, Li Y H, Yuan G T and Yao K F 2021 *Intermetallics* **131** 107116
[11] Li H X, Lu Z C, Wang S L, Wu Y and Lu Z P 2019 *Prog. Mater. Sci.* **103** 235
[12] Yoshizawa Y, Oguma S and Yamauchi K 1988 *J. Appl. Phys.* **64** 6044
[13] Ohta M and Hasegawa R 2017 *IEEE Trans. Magn.* **53** 2000205
[14] Wang W H, Zhao R, Han R, *et al.* 2025 *Mater. Futur.* **4** 033001
[15] Li H, Wang A, Liu T, Chen P B, He A, Li Q, Luan J H and Liu C T 2021 *Mater. Today* **42** 49
[16] Li X S, Zhou J, Shen L Q, Sun B A, Bai H Y and Wang W H 2023 *Adv. Mater.* **35** 2205863
[17] Hart G L W, Mueller T, Toher C and Curtarolo S 2021 *Nat. Rev. Mater.* **6** 730
[18] Schmidt J, Marques M R G, Botti S and Marques M A L 2019 *npj Comput. Mater.* **5** 83
[19] Ye Y F, Wang Q, Lu J, Liu C T and Yang Y 2016 *Mater. Today* **19** 349
[20] Stier S P, Kreisbeck C, Ihssen H, *et al.* 2024 *Adv. Mater.* **36** 2407791
[21] Rao Z Y, Tung P Y, Xie R W, *et al.* 2022 *Science* **378** 78
[22] Szymanski N J, Rendy B, Fei Y X, *et al.* 2023 *Nature* **624** 86
[23] Zhou Z Q, He Q F, Liu X D, Wang Q, Luan J H, Liu C T and Yang Y 2021 *npj Comput. Mater.* **7** 138
[24] Tang Y C, Wan Y, Wang Z Q, Zhang C, Han J N, Hu C H and Tang C Y 2022 *Mater. Des.* **219** 110726
[25] Pang B, Long Z L, Long T, He R, Liu X W and Pang M W 2023 *Mater. Des.* **231** 112054
[26] Lu Z C, Chen X, Liu X J, Lin D Y, Zhang Y B, Wang H, Jiang S H, Li H X, Wang X Z and Lu Z P 2020 *npj Comput. Mater.* **6** 187
[27] Ruder S 2017 arXiv:1706.05098 [cs.LG]
[28] Caruana R A 1993 *Proceedings of the Tenth International Conference on Machine Learning*, June 27–29, 1993, Amherst, MA, USA, pp. 41–48
[29] Ling F H, Luo J J, Li Y, Tang T, Bai L, Ouyang W L and Yamagata T 2022 *Nat. Commun.* **13** 7681
[30] Wu Y D, Zhu Y, Wang Y X and Chiribella G 2024 *Nat. Commun.* **15** 8796
[31] Tolstikhin I, Bousquet O, Gelly S and Schölkopf B 2017 *arXiv:1711.01558* [stat.ML]
[32] Deb K and Jain H 2014 *IEEE Trans. Evol. Comput.* **18** 577
[33] Gretton A, Borgwardt K, Rasch M J, Schölkopf B and Smola A J 2012 *J. Mach. Learn. Res.* **13** 723
[34] Jazzbin J 2020 Geatpy: The Genetic and Evolutionary Algorithm Toolbox With High Performance in Python.
[35] Zeni C, Pinsler R, Zügner D, *et al.* 2025 *Nature* **639** 624
[36] Belkina A C, Ciccolella C O, Anno R, Halpert R, Spidlen J and Snyder-Cappione J E 2019 *Nat. Commun.* **10** 5415
[37] Yang A, Su Y, Wang Z H, Jin S M, Ren J Z, Zhang X P, Shen W F and Clark J H 2021 *Green Chem.* **23** 4451
[38] Saha B, Gupta S, Phung D and Venkatesh S 2015 *Knowl. Inf. Syst.* **46** 315
[39] Lever J, Krzywinski M and Altman N 2017 *Nat. Methods* **14** 641
[40] Guo W H, Wu Y, Shi L X, Jia J L, Wang R B, Bu H T, Zhu Z F, Shao Y and Yao K F 2025 *Acta Mater.* **285** 120643
[41] Ohta M and Yoshizawa Y 2011 *J. Phys. D: Appl. Phys.* **44** 064004
[42] Yu M and Kakehashi Y 1994 *Phys. Rev. B* **49** 15723
[43] Yang S Y, Zang B W, Xiang M L, Shen F Y, Song L J, Gao M, Zhang Y, Huo J T and Wang J Q 2025 *Adv. Funct. Mater.* **35** 2425588
[44] Takeuchi A and Inoue A 2005 *Mater. Trans.* **46** 2817
[45] Huang B, Yang Y, Wang A D, Wang Q and Liu C T 2017 *Intermetallics* **84** 74
[46] Zhou Z Q, Shang Y H, Liu X D and Yang Y 2023 *npj Comput. Mater.* **9** 15
[47] Long T, Zhang Y, Fortunato M N, Shen C, Dai M and Zhang H B 2022 *Acta Mater.* **231** 117898
[48] Li Z and Birbilis N 2024 *npj Comput. Mater.* **10** 112
[49] Zhang Y X, Xie S J, Guo W, Ding J, Poh L H and Sha Z D 2023 *J. Alloy. Compd.* **960** 170793
[50] Wang Y H, Tian Y F, Kirk T, Laris O, Ross Jr J H, Noebe R D, Keylin V and Arroyave R 2020 *Acta Mater.* **194** 144
[51] Li X, Shan G C, Zhang J L and Sheck C H 2022 *J. Mater. Chem. C* **10** 17291
[52] Li X W, Chang L, Cao Y, Lu J Q, Lu X L and Jiang H Q 2023 *Proc. Natl. Acad. Sci. USA* **120** e2309062120
[53] Lundberg S M and Lee S I 2017 arXiv:1705.07874 [cs.AI]
[54] Han Y, Ding J, Kong F L, Inoue A, Zhu S L, Wang Z, Shalaan E, Al-Marzouki F 2017 *J. Alloy. Compd.* **691** 364
[55] Williams A, Moruzzi V, Malozemoff A and Terakura K 1983 *IEEE Trans. Magn.* **19** 1983
[56] Zang B, Parsons R, Onodera K, Kishimoto H, Kato A, Liu A C Y and Suzuki K 2017 *Scr. Mater.* **132** 68
[57] Suzuki K, Parsons R, Zang B, Onodera K, Kishimoto H, Shoji T and Kato A 2018 *J. Alloy. Compd.* **735** 613
[58] Xie L, Liu T, He A, Li Q, Gao Z K, Wang A, Chang C T and Wang X X 2017 *J. Mater. Sci.* **53** 1437
[59] Hou L, Fan X, Wang Q Q, Yang W M and Shen B L 2019 *J. Mater. Sci. Technol.* **35** 1655
[60] Naohara T 1996 *Metall. Mater. Trans. A* **27** 3424
[61] Xu J, Yang Y Z, Li W and Chen X C 2016 *J. Non-Cryst. Solids* **447** 167
[62] Zhang X Y, Huang X Y, Liang Y W, Cai Y F, Chen Y A, Gao M, Kawazoe Y, Umetsu R, Xiang M L, Zhao X J, Wang Y C, Wang J Q and Zhang Y 2024 *J. Alloy. Compd.* **1005** 176172